

Article

Heat Treatment Process, Microstructure, and Mechanical Properties of Spring Steel with Ultra-High Strength and Toughness

Fang Shi ¹, Jian Zheng ², Jie Zhang ², Yang Zhao ³  and Liqing Chen ^{1,*}

¹ State Key Laboratory of Rolling and Automation, Northeastern University, Shenyang 110819, China; fionaround13@gmail.com

² Hunan Valin Xiangtan Iron and Steel Co., Ltd., Xiangtan 411100, China

³ School of Materials Science and Engineering, Northeastern University, Shenyang 110819, China

* Correspondence: lqchen@mail.neu.edu.cn

Abstract: In this research, a new type of spring steel with ultra-high strength and toughness was designed, and its mechanical properties and microstructure under different heat treatment processes were studied. The results show that the optimal heat treatment process for the steel is oil quenching at 890 °C for 40 min, followed by tempering at 400 °C for 1 h. Its mechanical properties have an optimal combination of 1865MPa tensile strength, a yield strength of 1662 MPa, an elongation of 11.5%, a cross-sectional shrinkage of 51.5%, and a Charpy impact energy of 43.7 J at room temperature. With increasing austenitizing temperature, the austenite grain size increases, the martensite lath becomes thicker, and the strength decreases. With increasing tempering temperature, the lath boundary of martensite becomes blurred, the strength decreases, and the plasticity improves. In addition, it was found that during tempering at higher temperature (450 °C), large particle inclusions and secondary cracks appeared in the fractured surface, and a large number of carbides precipitated, leading to the brittleness of tempered martensite.

Keywords: spring steel; strengthening and toughening; heat treatments; tempered martensite embrittlement; retained austenite; large-angle grain boundaries



Citation: Shi, F.; Zheng, J.; Zhang, J.; Zhao, Y.; Chen, L. Heat Treatment Process, Microstructure, and Mechanical Properties of Spring Steel with Ultra-High Strength and Toughness. *Metals* **2024**, *14*, 180. <https://doi.org/10.3390/met14020180>

Academic Editors: Koh-ichi Sugimoto and Tomohiko Hojo

Received: 29 December 2023

Revised: 21 January 2024

Accepted: 29 January 2024

Published: 1 February 2024



Copyright: © 2024 by the authors. Licensee MDPI, Basel, Switzerland. This article is an open access article distributed under the terms and conditions of the Creative Commons Attribution (CC BY) license (<https://creativecommons.org/licenses/by/4.0/>).

1. Introduction

Developments in the automobile industry have caused serious problems in terms of energy consumption and environmental pollution, so the need for lightweight components is becoming more important. It has been reported [1] that using high-strength leaf springs is an effective way to achieve weight reductions in the automobile industry. At the same time, considering the harsh service environment and complex force situations of springs, it is necessary to pursue super-high strength materials that also have good mechanical properties and high impact toughness, so that vehicles can better absorb and disperse vibrations and impacts on the road during driving. Therefore, developing spring steel with ultra-high strength and toughness is an important research direction for automotive leaf springs.

It is well known that the main methods for developing spring steel with high strength and toughness include adjusting its alloy composition [2], microalloying [3–5], and optimizing heat treatment processes [6]. Over the years, the heat treatment process has evolved from traditional quenching and tempering (Q–T) to quenching and partitioning (Q–P); on this basis, various heat treatment methods based on Q–P technology have been developed to achieve better mechanical properties for spring steel [7]. Currently, medium- and high-carbon silicon spring steels such as 55SiCr [8], 54SiCrV [9], and 60Si2MnA [10] have been commercially used as suspension springs. Some typical studies, for example, Ma et al. [11], developed ultra-high strength spring steel (>2000 MPa) by adding microalloying elements such as Nb, V, and Ti to 55SiCr steel, and utilizing the precipitation behavior of carbonitrides. Chen et al. [12] obtained a new high strength spring steel with a tensile

strength and elongation of 2021 MPa and 10.3%, respectively, by implementing a series of heat treatment processes on 55SiCrVNb. Several studies [2,12–14] have shown that the yield strength of spring steel mainly comes from dislocation strengthening and precipitation strengthening. However, the increase in strength causes some decrease in toughness. The ultra-high strength spring steel mentioned in Ref. [13] has a tensile strength of 2002 MPa, a yield strength of 1775 MPa, an elongation of 11.1%, a reduction in area of 47%, but an impact energy of only 38 J. In addition, studies such as Refs. [15,16] have shown that the tensile strength of 50CrMnSiVNb spring steel with an elongation of 10% is approximately 1700 MPa, but the highest impact energy does not exceed 40 J. It is worth noting that the second-phase particles in steel have a different hardness from the matrix, and when deformation occurs, they do not coordinate with the matrix deformation, leading to stress concentration around carbides and deterioration in impact behavior [17]. Study [18] has shown that adding rare earth elements to steel can change the quantity and size of inclusions and carbides, reduce the adverse effects of impurity elements in steel, refine grains, reduce interface energy, and improve impact toughness. Xia et al. [16] found that the segregation formed by Mn in the microstructure is more likely to lead to the formation of cleavage surfaces, resulting in a decrease in impact toughness. Some studies [17,19] revealed that adding a certain amount of Ni can effectively improve toughness. Film-like residual austenite can hinder crack propagation and improve toughness [20]. Atsushi Ito et al. [21] found that Mn reduces the rate of dislocation multiplication, thereby lowering the work hardening rate. A study by Zhang et al. [22] indicated that increasing the oil bath temperature during quenching can increase the amount of retained austenite, and also improve toughness. Research in Ref. [23] indicated that when the V content in steel is 0.1%, the proportion of high-angle grain boundaries is less affected by temperature. Considering the beneficial effect of large-angle grain boundaries on impact toughness, an appropriate amount of V is added in the composition design to make the experimental steel exhibit more stable impact toughness under the same conditions as much as possible. Jiang et al. [24] conducted a study on the influence of different Nb contents on the microstructure evolution and impact behavior of M/A, and found that an increase in Nb content leads to an increase in the proportion of M/A components, and a decrease in the crack initiation energy. Further analysis revealed that an increase in the proportion of M/A components has a certain adverse effect on impact toughness. This makes it necessary to consider both the contribution of Nb (C, N) formed by Nb to the strength of the steel, and its potential adverse effects on impact toughness when designing the alloy composition of the experimental steel. It was also found in Refs. [25,26] that cleavage cracks appear at large-angle grain boundaries such as original austenite grain boundaries, martensite lath boundaries, and martensite packet boundaries. Thus, it is believed that large-angle grain boundaries can effectively hinder the propagation of cleavage cracks. Li et al. [27] aimed to change the dissolution of carbides during the austenitization process by holding austenite below its critical transformation temperature, in order to obtain more uniform and fine second-phase particles, thereby improving impact toughness without sacrificing strength. Therefore, introducing large-angle grain boundaries by adjusting the heat treatment process and adding an appropriate amount of microalloying elements have also become important ways to improve the toughness of spring steel.

The heat treatment process of spring steel mainly involves quenching and medium-temperature tempering. It is well known that quenching and tempering temperatures directly affect the strength and ductility of spring steel. The austenitizing temperature can affect the grain size, number of carbides, and proportion of large-angle grain boundaries. During the tempering process, the martensite structure undergoes recovery, while the retained austenite decomposes, and the size, quantity, and distribution of carbides in steel change. In addition, even small changes in alloy composition can alter the processing parameters of the optimal heat treatment. Therefore, it is necessary to explore the heat treatment process of spring steel with different contents of microalloying elements, in order to guide industrial production.

Although significant progress has been made in the research of ultra-high strength steel, the improvements in toughness have not been significant. On the basis of 55SiCrVNb steel, in this research, we designed a new type of high-strength and high-toughness spring steel by lowering the C and Mn contents, and increasing the Ni content. The quenching and tempering heat treatment was studied, and the influence of different heat treatment conditions on the microstructure, mechanical properties of the steel taken were taken into account. The aim of this study is to clarify the optimal heat treatment process for this new type of spring steel under this chemical composition, so that it can possess both ultra-high strength and toughness for future applications.

2. Experimental

The chemical composition of the designed spring steel is listed in Table 1. The ingot was firstly smelted in a medium-frequency vacuum induction furnace (150 kg capacity), and then forged at 1200 °C to obtain a billet (150 mm × 150 mm in cross section). After that, the billet was heated to 1200 °C in a resistance furnace and soaked for 3 h. Finally, a two-roll reversible hot rolling mill (φ450 mm) was used for the subsequent two-stage controlled rolling. The first stage of rolling began at 1050 °C, with a final thickness of 20 mm after 9 passes of rolling, and then it was air cooled to 850 °C for the second stage of rolling. After 5 passes of rolling, a thickness of 12 mm plate was obtained and air cooled to room temperature. The final rolling temperature was 800 °C.

Table 1. Chemical composition of the experimental steel (in wt pct).

C	Si	Mn + Cr + Ni	Ti + Nb + V	Al	S	P	Fe
0.38	1.47	2.20	0.16	0.048	0.0045	0.0033	Bal.

Based on the chemical composition of the experimental steel, combined with relevant empirical Formulas (1)–(3), preliminary predictions were made for the critical transformation temperatures of austenite A_{c3} and A_{c1} , as well as the martensitic transformation temperature M_s [28].

$$A_{c1} = 723 - 26Si + 20Cr + 55V - 18Ni - 12Mn \quad (1)$$

$$A_{c3} = 910 - 320C - 14Ni - 10Mn + 5Cr + 5V + 18Si \quad (2)$$

$$M_s = 520 - 320C - 50Mn - 30Cr - 20Ni - 5Si \quad (3)$$

According to the above formula, the theoretical A_{c1} of the experimental steel is 699 °C, A_{c3} is 809 °C, and M_s is 322 °C. The samples were heated to 860 °C, 890 °C, 920 °C, and 950 °C for 40 min, and then oil quenched to room temperature. After tempering at 400 °C for 1 h, they were water cooled to room temperature. The optimal austenitizing temperature was determined on the basis of the results of the mechanical properties test. The samples were labeled as Q860-T, Q890-T, Q920-T, and Q950-T. Tempering was carried out at 300 °C, 350 °C, 400 °C, and 450 °C for 1 h and then water cooled to room temperature. The corresponding samples were marked as Q-T300, Q-T350, Q-T400, and Q-T450, respectively. The heat treatment process is shown in Figure 1.

Three tensile specimens and three U-notch impact specimens were taken from the heat-treated steel plates. According to China national standard GB/T 228.1-2021, the room temperature tensile and impact specimens were processed and subjected to tensile tests at a tensile rate of 3 mm/min on the SANS-CMT5105 testing machine, and room temperature impact tests were conducted on the SANS-ZBC2452 pendulum impact testing machine. The ZEISS-ULTRA55 field emission scanning electron microscope (SEM) and its equipped electron backscatter diffraction (EBSD) system were used to observe the microstructure and impact fracture morphology, with a step size of 0.1 μm. After grinding with 240# to 1500# sandpaper and polishing with DNW2.5 water-soluble diamond grinding paste, a

4% nitric acid alcohol solution was used for corrosion. After grinding and polishing, the EBSD samples were vibration polished for 4 h with a frequency of 60 Hz. The polishing solution was a mixture of silica (50 nm) suspension and water (1:1 in volume). The amount of retained austenite in the tempered samples was quantitatively analyzed using a Smart Lab (Cu target) X-ray diffractometer (XRD), and the procedure used for XRD sample preparation is similar to that of the EBSD sample.

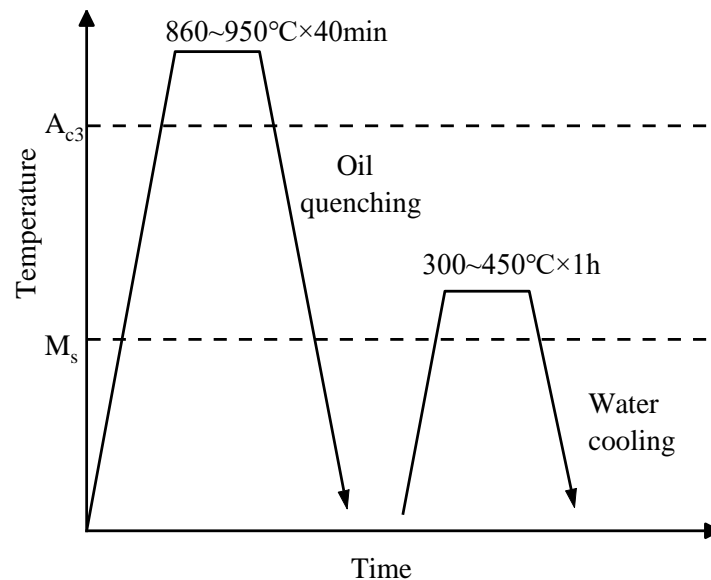


Figure 1. Schematic diagram of heat treatment process.

3. Results and Discussion

3.1. Microstructure

3.1.1. Effect of Austenitizing Temperature on Microstructure

Figure 2 shows the matrix microstructure of the sample quenched at 860 °C~950 °C and tempered at 400 °C, which consists of lath martensite and a small martensite–austenite island (M/A) made of retained austenite (consistent with the organizational characteristics in reference [7]). When the austenitizing temperature is lower than 920 °C, there are undissolved carbides (red circle) between the martensite laths and the boundary of martensite laths becomes blurred, as can be seen in Figure 2a,b. When the austenitizing temperature is increased to 920 °C or above, the carbides between the laths become greatly reduced, and the lath boundaries gradually become clearer. The laths in the martensite blocks tend to be arranged in parallel, the original austenite grain size increases, and the martensite laths become coarser. As the austenitizing temperature increases, the degree of undercooling increases, and the phase transformation temperature decreases, resulting in an increase in retained austenite during quenching (black arrow).

3.1.2. Effect of Tempering Temperature on Microstructure

Figure 3 shows SEM microstructures of the experimental steel quenched at 890 °C and tempered at 300 °C~450 °C, characterized by tempered troostite. Due to the decomposition of martensite, the dissolvable carbon atoms are ordered, resulting in the precipitation of carbides from the supersaturated martensite. Increasing the tempering temperature can lead to an increase in the width of the martensite plate, and an increase in the precipitation of carbides [29]. From Figure 3a–d, it is clear that the lath M recovers, the lath boundaries gradually dissolve, and the lamellar spacing increases.

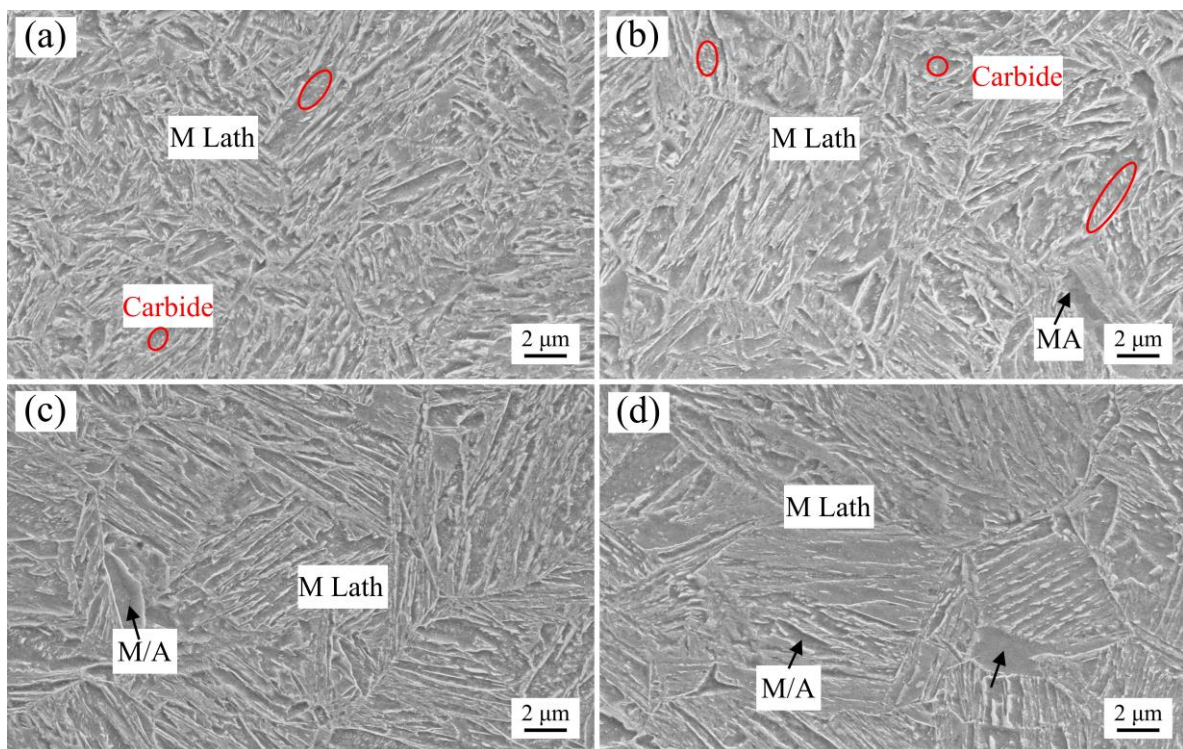


Figure 2. SEM micrographs of the experimental steel after quenching at different temperatures and tempering at 400 °C. (a) Q860-T; (b) Q890-T; (c) Q920-T; (d) Q950-T.

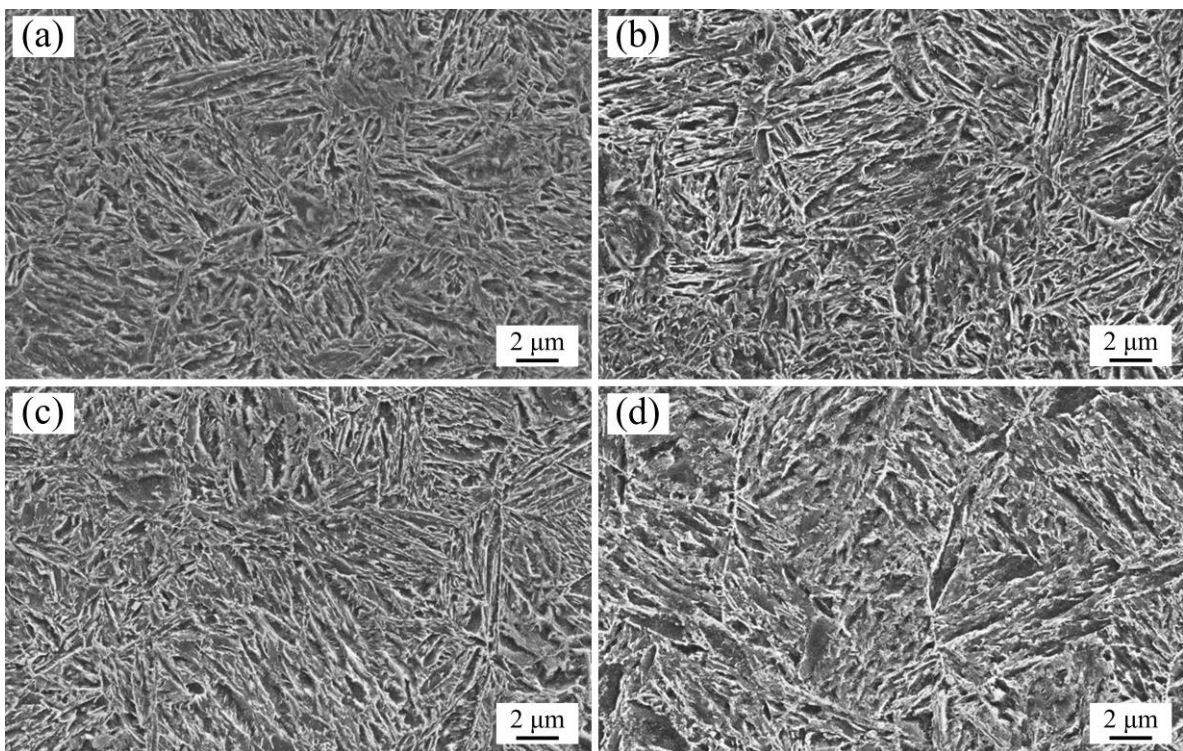


Figure 3. SEM micrographs of the experimental steel after quenching at 890 °C and tempering at different temperatures: (a) Q-T300 (b) Q-T350; (c) Q-T400; (d) Q-T450.

Figure 4a shows the XRD diffraction pattern of the experimental steel after tempering at different temperatures. The amount of retained austenite V_γ and the carbon content C_γ in the

retained austenite in Figure 4b are obtained from the diffraction results and Equations (4)–(6). According to Equation (1), the volume fraction of retained austenite (V_γ) can be calculated using the $(200)_\alpha$, $(211)_\alpha$, $(200)_\gamma$, $(220)_\gamma$, and $(311)_\gamma$ diffraction peaks [30]:

$$V_\gamma = 1.4I_\gamma / (I_\alpha + 1.4I_\gamma) \times 100\% \quad (4)$$

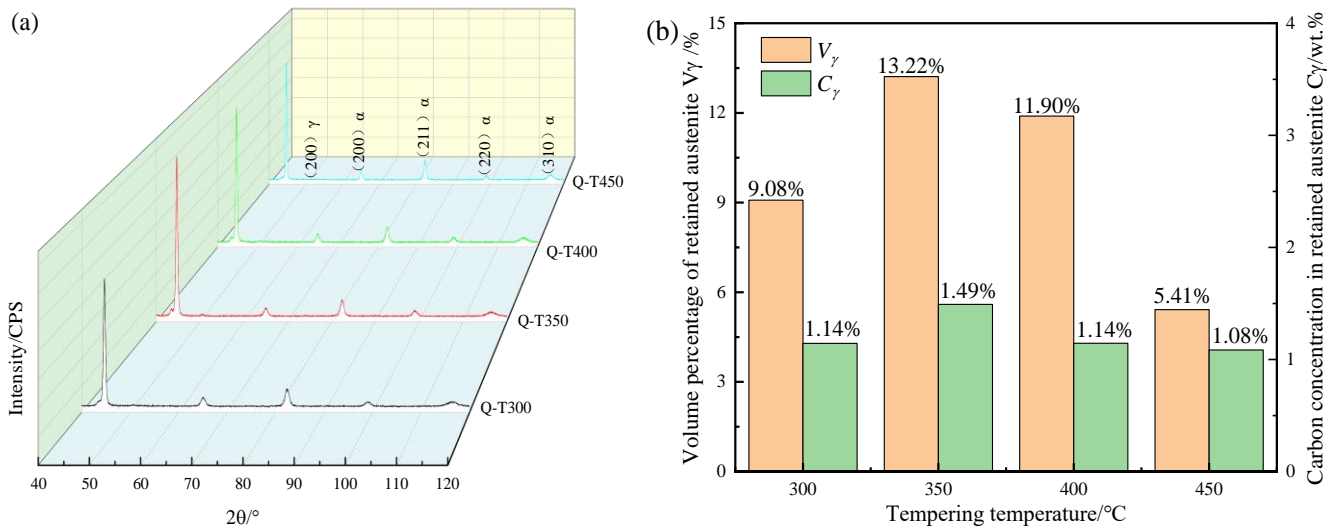


Figure 4. XRD results of the experimental steels after different treatments: (a) XRD patterns; (b) the volume percentage (V_γ) and average carbon concentration (C_γ) of the retained austenite.

I_α and I_γ in Equation (1) are the diffraction-integrated intensities of martensite and austenite, respectively. According to Equation (2), the carbon concentration (C_γ) in retained austenite can be calculated as follows [31]:

$$C_\gamma = (\alpha_\gamma - 3.547) / 0.046 \times 100\% \quad (5)$$

In Equation (2), α_γ is the average lattice parameter of retained austenite. Using Equation (6), α_γ is calculated through the diffraction angle and the corresponding $[hkl]$ diffraction [30]. λ is the diffraction wavelength.

$$A_\gamma = \lambda(h^2 + k^2 + l^2)^{1/2} / 2\sin\theta \quad (6)$$

It can be seen from Figure 4 that when the tempering temperature increases from 300 °C to 350 °C, the amount of retained austenite V_γ increases from 9.08% to 13.22%; the corresponding carbon content in the retained austenite increases from 1.14% to 1.49%, with a relatively small increase. When the tempering temperature increases beyond 350 °C, the retained austenite content decreases and the carbon content also decreases.

3.2. Mechanical Properties

Figure 5 shows the engineering stress–strain curves of experimental steel under different heat treatment processes, and their mechanical performance data are listed in Table 2. From Table 2, it can be seen that as the austenitizing temperature increases, the tensile strength and yield strength both decrease. The elongation and cross-sectional shrinkage of the Q890-T specimen remain relatively high compared to the other specimens. When the austenitizing temperature exceeds 890 °C, the elongation gradually decreases. The performance requirements for the experimental steel used in this article are as follows: yield strength >1450 MPa, tensile strength >1650 MPa, elongation \geq 12%, reduction in area \geq 40%, and impact energy (KU2) \geq 40 J at 20 °C. Therefore, although the strength indicators under all quenching conditions meet the requirements, considering the elongation, 890 °C is considered the optimal austenitizing temperature. Thus, tempering experiments were conducted at this temperature.

As shown in Table 2, with the increase in tempering temperature, the yield strength and tensile strength decrease to 1635 MPa and 1861 MPa, respectively. The elongation first decreased and then increased, while the cross-sectional shrinkage first increased and then decreased. However, the overall trend was upward, increasing from 10.8% and 47.1% to 12.7% and 51.1%, respectively, and the proportion of improvement in elongation is 17.6%.

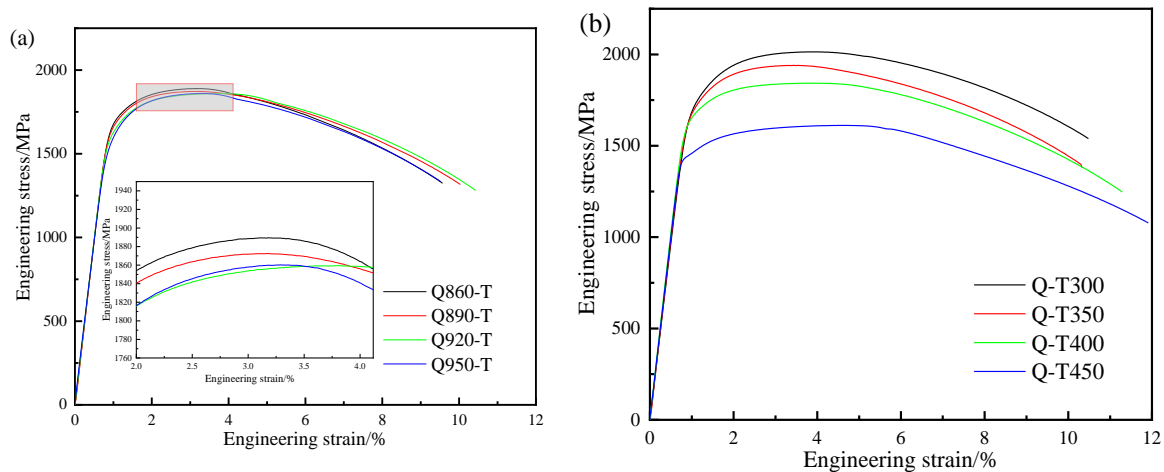


Figure 5. The engineering stress–strain curves of the experimental steel for different austenitizing temperatures and tempering temperatures. (a) Austenitizing temperature and (b) tempering temperature.

Table 2. Mechanical properties of the experimental steel under different heat treatments.

Sample	YS (MPa)	TS (MPa)	TEL (%)	RA (%)
Q860-T	1700	1888	10.1	49.7
Q890-T	1662	1865	11.1	51.5
Q920-T	1635	1862	10.4	51.5
Q950-T	1633	1858	10.0	51.1
Q-T300	1735	2020	10.8	47.1
Q-T350	1713	1953	10.3	48.2
Q-T400	1662	1865	11.5	51.5
Q-T450	1635	1861	12.7	51.1

3.3. Impact Toughness

The room temperature Charpy impact energy at different tempering temperatures was plotted in Figure 6, which shows that as the tempering temperature increases, the impact energy has a wavy decreasing trend. The impact energies absorbed for the Q-T300 and Q-T400 specimens are 44.2 J and 43.7 J, respectively. The two values are very close. When the tempering temperature is 450 °C, the impact energy shows a significant decrease, dropping to 35.4 J. Based on this inference, it is possible that there may be structural defects in the steel that have an adverse effect on its toughness, such as large particle inclusions. Figure 7 shows the impact fracture morphology of experimental steel after tempering at different temperatures. In Figure 7a,c, there are numerous cleavage planes (black arrows) and a small number of smaller and shallower dimples, with a few micropores (yellow circles) and cleavage steps (white arrows). In Figure 7b, in addition to a small number of ductile dimples and a large number of cleavage planes, there are also secondary cracks (white circles) and holes formed by the drop of large particle inclusions (red circles), which lead to a decrease in the impact energy to 41.9 J; in Figure 7d, a large number of cleavage planes are distributed, with almost no dimples observed. At the same time, secondary cracks and large-sized pores appear, which further deteriorate the impact toughness. Figure 8 shows the GB graph of the experimental steel after tempering at different temperatures, and Figure 9 shows the statistical graph of the proportion of grain boundaries in different

tempered samples. According to the scatter plot in Figure 9, the Q-T350 sample has the highest proportion of high-angle grain boundaries at 74.9%, while the proportion of high-angle grain boundaries in the other samples is around 71%, with little difference. Through comprehensive consideration of mechanical properties and impact toughness, it can be considered that 400 °C is the optimal tempering temperature.

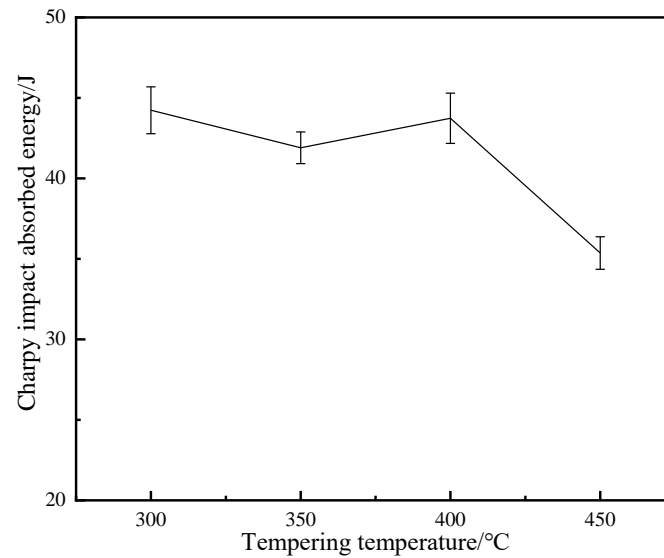


Figure 6. The impact absorbed energy of the experimental steel tempered at different temperatures after austenitizing at 890 °C.

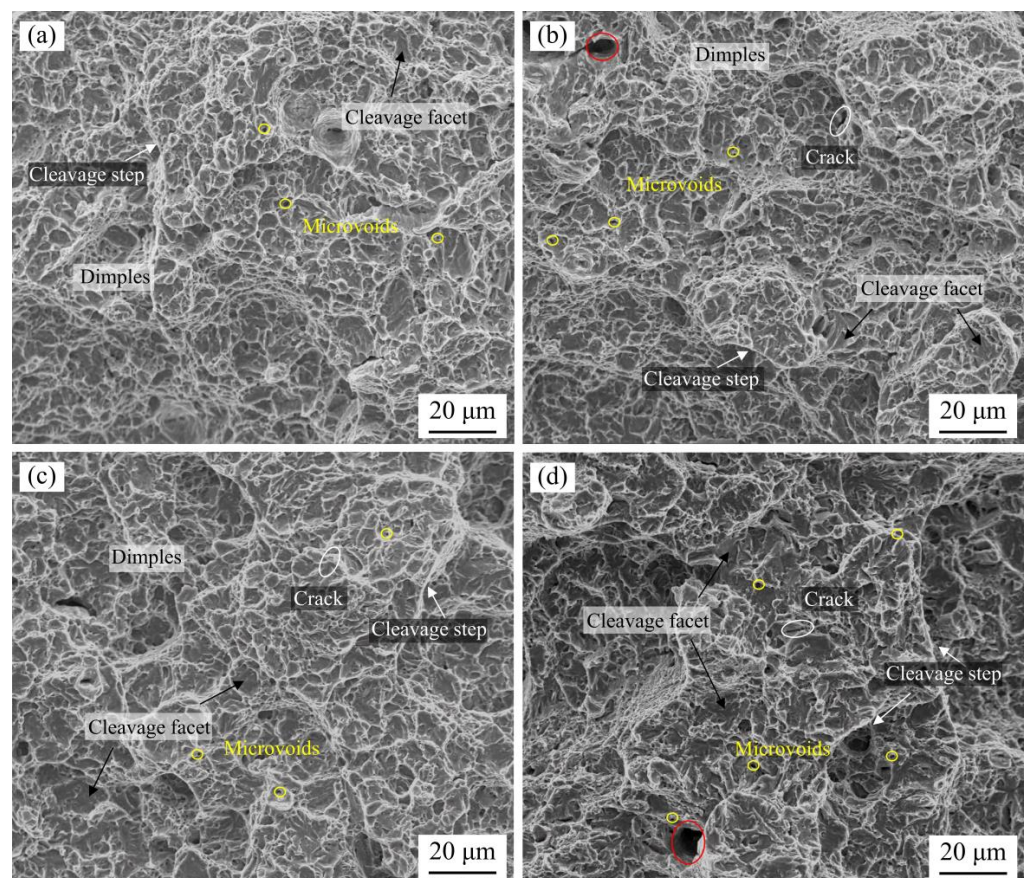


Figure 7. SEM micrographs of the impact fracture surfaces. (a) Q-T300; (b) Q-T350; (c) Q-T400; (d) Q-T450.

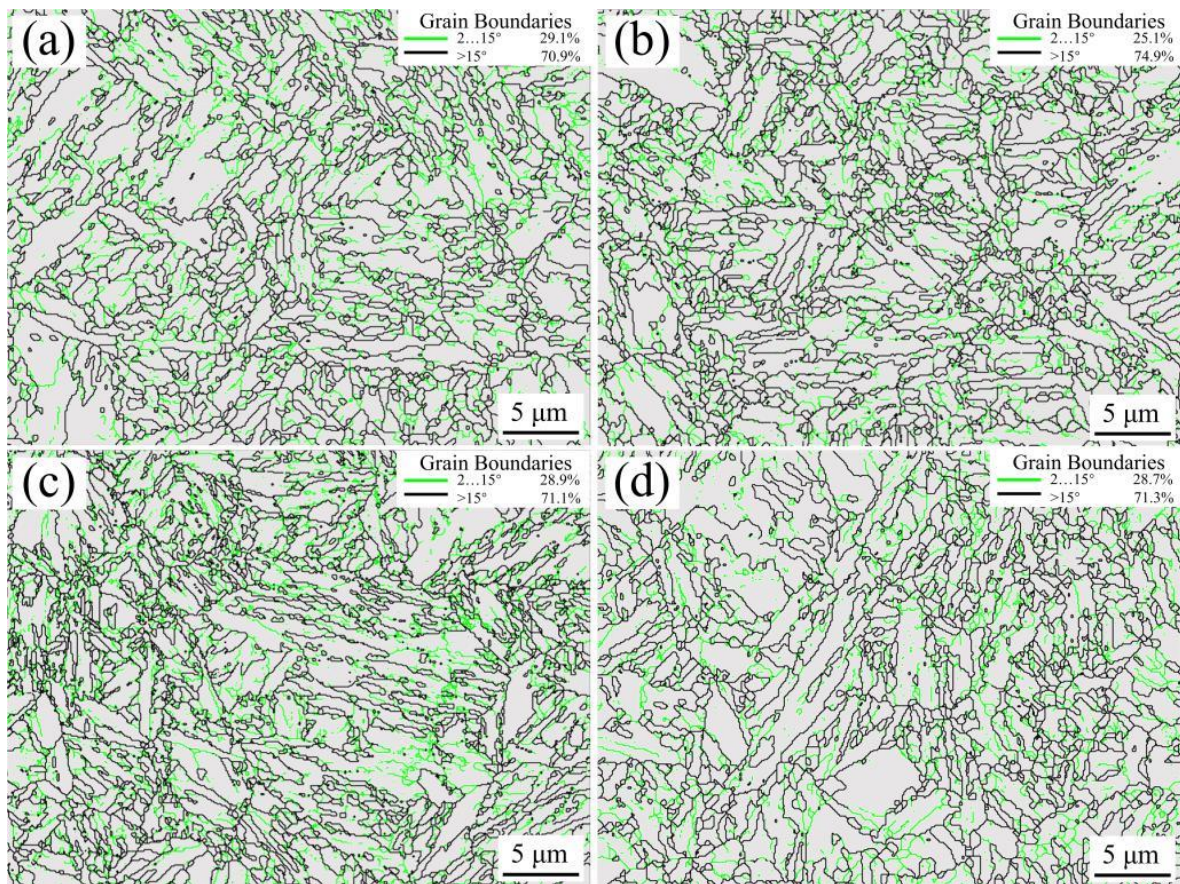


Figure 8. EBSD results of the experimental steels. (a) Q-T300; (b) Q-T350; (c) Q-T400; (d) Q-T450.

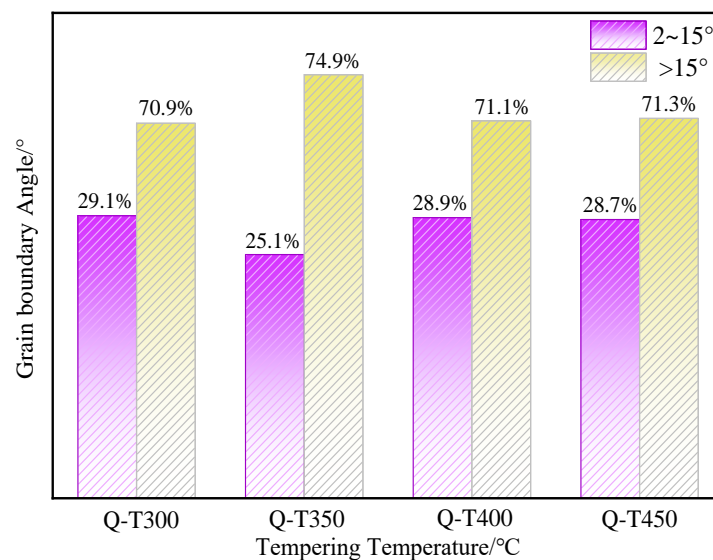


Figure 9. Statistical diagram of grain boundary proportions after tempering at 300 °C~450 °C.

4. Discussion

The microstructure after quenching treatment is mainly parallel-arranged lath martensite. As the austenitizing temperature increases, the lath arrangement gradually becomes parallel, the width increases, and the length increases. This is because as the temperature increases, the thermal activation energy in steel increases [4], making carbon atoms more active to diffuse faster from inside the grains to near the grain boundaries, prompting the

growth of austenite grains. In addition, the driving force of the martensitic transformation comes from the free energy difference between the old and new phases [32]. Therefore, as the heating temperature increases, the degree of undercooling generated during quenching increases. The resulting nucleation driving force increases, causing the phase transformation to occur more rapidly; thus, the lath size increases and the strength decreases. In addition, M/A is a soft phase, and an increase in the M/A island content will also reduce the strength of the high-temperature quenched samples.

After tempering, the structure mainly undergoes martensite recovery, carbide precipitation, and decomposition of the retained austenite. As we all know, the high-density dislocations in martensite recover during the tempering process, and the dislocations are reduced. As the tempering temperature increases, the degree of dislocation recovery increases, thereby reducing the yield strength of the material. The specific dislocation density can be imported into Topas 7 software from the XRD diffraction results for fitting calculation. The dislocation densities of the Q-T300~Q-T450 were found to be $6.26 \times 10^{15} \text{ m}^{-2}$, $5.23 \times 10^{15} \text{ m}^{-2}$, $4.23 \times 10^{15} \text{ m}^{-2}$, and $3.29 \times 10^{15} \text{ m}^{-2}$, respectively, which can be obtained by substituting them into Equation (7) to obtain the contribution of dislocation strengthening σ_p [33]:

$$\sigma_p = \alpha M_d G b \sqrt{\rho} \quad (7)$$

The calculated data are listed in Table 3, and the obtained data are consistent with the actual performance.

Table 3. Dislocation density and dislocation strengthening values of different tempered samples.

Sample	Q-T300	Q-T350	Q-T400	Q-T450
$\rho \text{ (m}^{-2}\text{)}$	6.26×10^{15}	5.23×10^{15}	4.23×10^{15}	3.29×10^{15}
$\sigma_p \text{ (MPa)}$	1177.5	1076.1	967.8	853.5

Liu et al. [34] found that the tempering process causes the precipitation and transformation of carbides in martensite. The silicon content has an important influence on the decomposition or transformation temperature of ϵ -carbide. Some studies, such as Refs. [35,36] indicated that silicon elements have a certain inhibitory effect on the decomposition of ϵ -carbide and cementite transformation. That is to say, the content of Si element is related to the transformation temperature of ϵ -carbide, and shows a synchronous change pattern. In low alloy steel (silicon content 1.6%) studied by Kozeschnik et al. [22], ϵ -carbide begins to transform into cementite at the tempering temperature of 260 °C. The Si content of the steel in this experiment is 1.46% (mass percentage), so in the Q-T300 sample, the precipitation and transformation of ϵ -carbide occur simultaneously. This process in steel causes the carbon concentration in the supersaturated martensite to decrease, and the cementite content to increase. The calculation formula (8) [13] of solid solution strengthening is as follows:

$$\sigma_{ss} = 4570 \text{ C}\% + 83\text{Si}\% + 37\text{Mn}\% - 30\text{Cr}\% \quad (8)$$

According to the formula, a decrease in carbon concentration leads to a weakening of solid solution strengthening; the precipitation of cementite increases the contribution of precipitation strengthening, but it cannot make up for the loss of dislocation strengthening. Therefore, it can be considered that the weakening of dislocation strengthening due to martensite recovery is the main reason for the decrease in strength as the tempering temperature increases.

During tempering, the retained austenite and its carbon content also undergo dynamic changes. When the tempering temperature increases from 300 °C to 350 °C, the carbon atoms in the supersaturated martensite diffuse into the untransformed austenite, increasing its stability; thus, so the retained austenite content increases [37,38]. When the tempering temperature is higher than 350 °C, the microalloying elements diffuse, causing the precipitation of carbides to increase, the carbon content to decrease, the M_s point to

increase, and the retained austenite to decompose. Research in Ref. [39] has shown that film-like retained austenite can hinder crack propagation and improve toughness. When the tempering temperature increases from 400 °C to 450 °C, the retained austenite content is the lowest, only 5.41%, and the number of carbide precipitations in the matrix is the largest. When subjected to impact deformation, the precipitation of carbides is inconsistent with the deformation of the matrix, which can easily cause cracks. Moreover, the residual austenite content and the number of high-angle grain boundaries are small, making it difficult to hinder the expansion of cracks. Figure 8d shows that there are holes formed by the falling of large particle inclusions, a large number of cleavage planes, and tearing edges on the impact fracture surface. The impact energy is greatly reduced to 35.4 J, and tempered martensitic brittleness appears at this time.

5. Conclusions

In this study, a new high-strength and high-toughness spring steel with a tensile strength of approximately 1800 MPa was developed and characterized using SEM, XRD, and EBSD, and the optimal heat treatment process of this steel grade was obtained based on an evaluation of its mechanical properties and microstructure. The following conclusions can be drawn:

- (1) The optimal heat treatment process is oil quenching at 890 °C for 40 min, followed by tempering at 400 °C for 60 min, and then water cooling. Under such processing conditions, this spring steel has high strength and high plasticity. Its tensile strength reaches 1865 MPa, its yield strength is 1662 MPa, its elongation is 11.5%, its area shrinkage is 51.5%, and its impact toughness reaches 43.7 J.
- (2) After quenching, the microstructure of this spring steel is mainly composed of lath martensite and a small amount of retained austenite. As the austenitizing temperature increases, the size of martensite laths increases, and the amount of martensite and M/A increase, which is the main reason for the decrease in strength. After tempering, this spring steel mainly undergoes martensite recovery, resulting in a reduction in dislocation density. This is the main reason for the decrease in strength caused by an increase in tempering temperature.
- (3) In different tempering temperature ranges, the atomic diffusion capabilities in steel are different, causing the amount of retained austenite to first increase, and then decrease. At 450 °C, the steel exhibits tempered martensitic brittleness due to the massive decomposition of retained austenite and the precipitation of carbides.

Author Contributions: Data curation, F.S.; investigation, J.Z. (Jian Zheng) and J.Z. (Jie Zhang); methodology, J.Z. (Jian Zheng) and J.Z. (Jie Zhang); project administration, L.C.; writing—original draft, F.S.; writing—review and editing, L.C. and Y.Z. All authors have read and agreed to the published version of the manuscript.

Funding: This work was financially supported by the research and development project from Hunan Valin Xiangtan Iron and Steel Co., Ltd. under contract No. 2022040200031.

Data Availability Statement: The raw data supporting the conclusions of this article will be made available by the authors on request.

Conflicts of Interest: Authors Jian Zheng and Jie Zhang were employed by the company Hunan Valin Xiangtan Iron and Steel Co., Ltd. The remaining authors declare that the research was conducted in the absence of any commercial or financial relationships that could be construed as potential conflicts of interest.

References

1. Senuma, T.; Okayasu, M.; Mohrbacher, H. Microstructural Control and Alloy Design for Improving the Resistance to Delayed Fracture of Ultrahigh-Strength Automotive Steel Sheets. *Metals* **2023**, *13*, 1368. [[CrossRef](#)]
2. Yuan, L.; You, X.; Liu, Z.; Zhang, J.; Hu, F.; Wang, K.; Chen, H.; Yang, Z.; Zhang, C. A new Nb-Si-added 2100 MPa ultra-strong spring steel designed under the guidance of a strength model. *J. Mater. Sci.* **2023**, *58*, 5933–5950. [[CrossRef](#)]

3. Zhang, C.; Zhou, L.; Liu, Y. Heredity in the Microstructure and Mechanical Properties of Hot-rolled Spring Steel Wire 60S12MnA during Heat Treatment Process. *J. Mater. Sci. Technol.* **2013**, *29*, 82–88. [[CrossRef](#)]
4. Xu, L.; Chen, L.; Sun, W. Effects of Soaking and Tempering Temperature on Microstructure and Mechanical Properties of 65Si2MnWE Spring Steel. *Vacuum* **2018**, *154*, 322–332. [[CrossRef](#)]
5. Cruz, J.A., Jr.; Rodrigues, T.F.M.; Viana, V.D.C.; Abreu, H.; Santos, D.B. Influence of Temperature and Time of Austempering Treatment on Mechanical Properties of SAE 9254 Commercial Steel. *Steel Res. Int.* **2012**, *83*, 22–31. [[CrossRef](#)]
6. Dai, Q.; Jin, L.; Chen, W.; Wu, J.; Fang, Z.; Yang, T.; Ma, R.; Li, K. High-performance reality of 55SiCrV spring steel processed by the rapid-induction heat treatment. *Mater. Sci. Technol.* **2023**, *39*, 1267–1277. [[CrossRef](#)]
7. Zurnadzhy, V.; Efremenko, V.; Wu, K.; Azarkhov, A.; Chabak, Y.; Greshta, V.; Isayev, O.; Pomazkov, M. Effects of stress relief tempering on microstructure and tensile/impact behavior of quenched and partitioned commercial spring steel. *Mater. Sci. Eng. A* **2019**, *745*, 307–318. [[CrossRef](#)]
8. Liu, Y.; Zhang, W.; Tong, Q.; Wang, L. Effects of Temperature and Oxygen Concentration on the Characteristics of Decarburization of 55SiCr Spring Steel. *ISIJ Int.* **2014**, *54*, 1920–1926. [[CrossRef](#)]
9. Barani, A.A.; Li, F.; Romano, P.; Ponge, D.; Raabe, D. Design of High-Strength Steels by Microalloying and Thermomechanical Treatment. *Mater. Sci. Eng. A* **2007**, *463*, 138–146. [[CrossRef](#)]
10. Zhang, C.; Liu, Y.; Zhou, L.; Jiang, C.; Xiao, J. Forming Condition and Control Strategy of Ferrite Decarburization in 60Si2MnA Spring Steel Wires for Automotive Suspensions. *Int. J. Miner. Metall. Mater.* **2012**, *19*, 116–121. [[CrossRef](#)]
11. Ma, X.; Huang, Z.; Yao, Z.; Jiang, Z.; Zhao, B. Strengthening Mechanisms of Microalloying Spring Steel. In Proceedings of the 2018 China Symposium on Sustainable Steelmaking Technology (CSST2018), Tianjin, China, 25–27 October 2018.
12. Chen, K.; Jiang, Z.; Liu, F.; Yu, J.; Li, Y.; Gong, W.; Chen, C. Effect of quenching and tempering temperature on microstructure and tensile properties of microalloyed ultra-high strength suspension spring steel. *Mater. Sci. Eng. Struct. Mater. Prop. Microstruct.* **2019**, *766*, 138272. [[CrossRef](#)]
13. Wang, S.; Xi, X.; Zhao, Y.; Chen, L. Microstructures and Mechanical Properties of an Ultrahigh-Strength and Ductile Medium-Carbon High-Silicon Spring Steel. *Steel Res. Int.* **2023**, *94*, 2200149. [[CrossRef](#)]
14. Chen, W.; Gao, P.; Wang, S.; Zhao, X.; Zhao, Z. Strengthening Mechanisms of Nb and V Microalloying High Strength Hot-Stamped Steel. *Mater. Sci. Eng. A* **2020**, *797*, 140115. [[CrossRef](#)]
15. Xia, B.; Zhang, P.; Wang, B.; Zhu, Y.K.; Li, X.W.; Zhang, Z.F. A simultaneous improvement of the strength and plasticity of spring steels by replacing Mo with Si. *Mater. Sci. Eng. A* **2021**, *820*, 141516. [[CrossRef](#)]
16. Xia, B.; Wang, B.; Zhang, P.; Li, X.; Zhang, Z. The effect of tempering temperature on the microstructure and impact properties of high-strength spring steel. *J. Mater. Res.* **2023**, *37*, 341–352.
17. Jiang, B.; Mei, Z.; Zhou, L.; Zhang, C.; Liu, Y. Microstructure Evolution, Fracture and Hardening Mechanisms of Quenched and Tempered Steel for Large Sized Bearing Rings at Elevated Quenching Temperatures. *Met. Mater. Int.* **2016**, *22*, 572–578. [[CrossRef](#)]
18. Hao, C.L.; Yang, C.Y.; Liu, P.; Luan, Y.K.; Sang, B.G. Effects of rare earth elements on inclusions, microstructure and impact toughness of spring steel. *J. Iron Steel Res. Int.* **2023**. [[CrossRef](#)]
19. Jiang, B.; Wu, M.; Zhang, M.; Zhao, F.; Zhao, Z.; Liu, Y. Microstructural Characterization, Strengthening and Toughening Mechanisms of a Quenched and Tempered Steel: Effect of Heat Treatment Parameters. *Mater. Sci. Eng. A* **2017**, *707*, 306–314. [[CrossRef](#)]
20. Chen, K.; Jiang, Z.; Liu, F.; Li, H.; Ma, X.; Zhao, B.; Kang, C.; Li, Y. Enhanced Mechanical Properties by Retained Austenite in Medium-Carbon Si-Rich Microalloyed Steel Treated by Quenching-Tempering, Austempering and Austempering-Tempering Processes. *Mater. Sci. Eng. A* **2020**, *790*, 139742. [[CrossRef](#)]
21. Ito, A.; Fuse, T.; Torizuka, S. Effect of Dislocation Behavior on High Strength and High Ductility of Low Carbon-2%Si-5%Mn Fresh Martensitic Steel. *Tetsu-to-Hagané* **2022**, *108*, 877–890. [[CrossRef](#)]
22. Zhang, L.; Gong, D.; Li, Y.; Wang, X.; Ren, X.; Wang, E. Effect of Quenching Conditions on the Microstructure and Mechanical Properties of 51CrV4 Spring Steel. *Metals* **2018**, *8*, 1056. [[CrossRef](#)]
23. Stornelli, G.; Tselikova, A.; Gattia, D.M.; Mortello, M.; Schmidt, R.; Sgambetterra, M.; Testani, C.; Zucca, G.; Di Schino, A. Influence of Vanadium Micro-Alloying on the Microstructure of Structural High Strength Steels Welded Joints. *Materials* **2023**, *16*, 2897. [[CrossRef](#)]
24. Jiang, J.; Zhang, Z.; Guo, K.; Guan, Y.; Yuan, L.; Wang, Q. Effect of Nb Content on the Microstructure and Impact Toughness of High-Strength Pipeline Steel. *Metals* **2024**, *14*, 42. [[CrossRef](#)]
25. Cui, J.; Zhu, W.; Chen, Z.; Chen, L. Effect of Simulated Cooling Time on Microstructure and Toughness of CGHAZ in Novel High-Strength Low-Carbon Construction Steel. *Sci. Technol. Weld. Join.* **2020**, *25*, 169–177. [[CrossRef](#)]
26. Dai, X.; Chen, Y.-F.; Wang, P.; Zhang, L.; Yang, B.; Chen, L.-S. Mechanical and fatigue properties of SA508-IV steel used for nuclear reactor pressure vessels. *J. Iron Steel Res. Int.* **2022**, *29*, 1312–1321. [[CrossRef](#)]
27. Li, Y.; Jiang, Z.; Wang, P.; Li, D.; Li, Y. Effect of a modified quenching on impact toughness of 52,100 bearing steels. *J. Mater. Sci. Technol.* **2023**, *160*, 96–108. [[CrossRef](#)]
28. Trzaska, J.; Dobrzański, L.A. Modelling of CCT diagrams for engineering and constructional steels. *J. Mater. Process. Technol.* **2007**, *192–193*, 504–510. [[CrossRef](#)]
29. Xie, Y.; Cheng, X.; Wei, J.; Luo, R. Characterization of Carbide Precipitation during Tempering for Quenched Dievar Steel. *Materials* **2022**, *15*, 6448. [[CrossRef](#)]

30. Van Dijk, N.; Butt, A.; Zhao, L.; Sietsma, J.; Offerman, S.; Wright, J.; van der Zwaag, S. Thermal Stability of Retained Austenite in TRIP Steels Studied by Synchrotron X-Ray Diffraction during Cooling. *Acta Mater.* **2005**, *53*, 5439–5447. [[CrossRef](#)]
31. Xi, X.; Wang, J.; Li, X.; Chen, L.; Wang, Z. The Role of Intercritical Annealing in Enhancing Low-Temperature Toughness of Fe-C-Mn-Ni-Cu Structural Steel. *Metall. Mater. Trans. Phys. Metall. Mater. Sci.* **2019**, *50*, 2912–2921. [[CrossRef](#)]
32. Li, Y.; Wang, L.; Zhu, K.; Wang, C.; Xu, W. An integral transformation model for the combined calculation of key martensitic transformation temperatures and martensite fraction. *Mater. Des.* **2022**, *219*, 110768. [[CrossRef](#)]
33. Liu, G.; Liu, K.; Zhang, M.; Ning, J.; Feng, Y. Effect of cold rolling reduction ratio on microstructure and mechanical properties of Fe–10Mn–4Al–0.4C steel containing δ ferrite. *Mater. Sci. Eng. A* **2023**, *867*, 144715. [[CrossRef](#)]
34. Liu, F.; Lin, X.; Song, M.; Yang, H.; Song, K.; Guo, P.; Huang, W. Effect of tempering temperature on microstructure and mechanical properties of laser solid formed 300M steel. *J. Alloys Compd.* **2016**, *689*, 225–232. [[CrossRef](#)]
35. Kim, B.; Celada, C.; San Martin, D.; Sourmail, T.; Rivera-Diaz-del-Castillo, P.E.J. The Effect of Silicon on the Nanoprecipitation of Cementite. *Acta Mater.* **2013**, *61*, 6983–6992. [[CrossRef](#)]
36. Kozeschnik, E.; Bhadeshia, H.K.D.H. Influence of Silicon on Cementite Precipitation in Steels. *Mater. Sci. Technol.* **2008**, *24*, 343–347. [[CrossRef](#)]
37. Dong, J.; Zhou, X.; Liu, Y.; Li, C.; Liu, C.; Guo, Q. Carbide precipitation in Nb-V-Ti microalloyed ultra-high strength steel during tempering. *Mater. Sci. Eng. A* **2017**, *683*, 215–226. [[CrossRef](#)]
38. Toji, Y.; Miyamoto, G.; Raabe, D. Carbon Partitioning during Quenching and Partitioning Heat Treatment Accompanied by Carbide Precipitation. *Acta Mater.* **2015**, *86*, 137–147. [[CrossRef](#)]
39. Zhou, C.; Ye, Q.B.; Hu, J.; Zhao, T.; Gao, X.H.; Wang, Z.D. Ultra-high-strength multi-alloyed steel with enhanced cryogenic toughness using thermally stable retained austenite. *Mater. Sci. Eng. A* **2022**, *831*, 142356. [[CrossRef](#)]

Disclaimer/Publisher’s Note: The statements, opinions and data contained in all publications are solely those of the individual author(s) and contributor(s) and not of MDPI and/or the editor(s). MDPI and/or the editor(s) disclaim responsibility for any injury to people or property resulting from any ideas, methods, instructions or products referred to in the content.